

# Characterization of a wind turbine wake evolving over an intertidal zone performed with dual-lidar observations

Changzhong Feng<sup>1</sup>, Bingyi Liu<sup>1</sup>, Songhua Wu<sup>1,2</sup>, Jintao Liu<sup>1</sup>, Rongzhong Li<sup>3</sup>, Xitao Wang<sup>3</sup>

<sup>1</sup>Ocean Remote Sensing Institute, Ocean University of China, Qingdao 266100, China

5 <sup>2</sup>Laboratory for Regional Oceanography and Numerical Modeling, Qingdao National Laboratory for Marine Science and Technology

<sup>3</sup>Seaglet Environmental Technology, Qingdao, China

*Correspondence to:* (liubingyi@ouc.edu.cn)

**Abstract.** As modern wind power industry quickly develops, it is of high priority to optimize layouts and operations of wind turbines to reduce the influences of wakes induced by upstream wind turbines. The wake behaves complicatedly with land-ocean-atmosphere interactions. The aim of this study is to observe this complex wake by two or more synchronously operated Doppler lidars. Accordingly, we characterized a wind turbine wake evolving over an intertidal zone performed with dual-lidar observations, in which a designed coplanar scanning mode was used to obtain the exactly match probing volume. The case that wake length on that day increased with rising tide was analysed in details. It suggested that, at least qualitatively, the increase of wake length varied with underlying surface roughness transition from mud to sea water as well as the rising sea level on that day. This phenomenon needs further wake measurements for several periods. Finally, wake meandering cases were analyzed in detail. Our research shows that the dual-lidar observation technology with designed coplanar scanning mode is a promising remote sensing tool for characterization of complicated wind turbine wakes.

## 1 Introduction

20 Wind energy is no doubt one of the most promising alternative energies. As wind power industry increases rapidly during the past decades, optimizations of wind turbines layouts and operations have presented a significant challenge to minimize the cost of energy. Specifically, considerably decreased output power and enhanced fatigue are induced by upstream turbine wakes (Baker and Walker, 1984; Barthelmie et al., 2003; Chowdhury et al., 2012). Therefore, various experiments and simulations have been performed previously in an attempt to investigate the dependence of the wake behaviours (velocity deficit, wake length, wake boundary and wake centreline) on the atmospheric conditions (wind speed, turbulence, surface roughness and atmospheric stability). Full-scale experiment could convincingly help the validation of large-eddy simulation (LES) technique combined with turbine model (Abkar and Porté-Agel, 2015; Iungo et al., 2013; Porté-Agel et al., 2011; Wu and Porté-Agel, 2012), and ultimately improve the prediction of wind power harvesting (Aitken and Lundquist, 2014; Fuertes et al., 2014; Hirth et al., 2012).

The conventional approach to obtain wind data at a fixed point is to utilize cup anemometers mounted on meteorological towers (Baker and Walker, 1984; Elliott and Barnard, 1990). However, the investigation of complex wake structure needs more data points. For instance, Elliott et al. analysed wake characteristics from wind data of nine meteorological towers (Elliott and Barnard, 1990). Nevertheless, the impact of towers with large cross-sections on the measurements at hub height  
5 should be taken into consideration. Therefore, the remote sensing technique such as lidar, radar, and sodar has been increasingly adopted in experimental turbine wake research. Högström et al. utilized four different equipments, including a kite anemometer, a tower-mounted instrumentation, a tethered balloon sounding and a Sonic Detection and Ranging (SODAR), to obtain the vertical profile of turbulence intensity (Högström et al., 1988). Kambezidis et al. employed three SODARs placed at equal distances downstream of a turbine to investigate velocity deficit, turbulence intensity and  
10 temperature structure within the wake (Kambezidis et al., 1990). In situ measurement combine with acoustic sounders was used to identify rotational motion inside the wake by Helmig et al. (Helmig et al., 1995). Barthelmie et al. elaborately evaluated the operation of the SODAR mounted on a ship for measuring offshore wind turbine wake, and quantified the relationship between wind farm efficiency and various atmospheric conditions (Barthelmie et al., 2003; Barthelmie and Jensen, 2010).

15 For a pulsed coherent Doppler lidar (PCDL), access to the full-scale wind turbine wake could be provided by a variety of geometrical scanning modes (Bingöl et al., 2010; Kähler et al., 2010; Trujillo et al., 2011; Wu et al., 2016; Wu et al., 2014). The lidar deployment and wind direction should be taken into account because lidar directly obtains Light of Sight (LOS) velocity. For instance, the lidar-turbine line should be strictly aligned with the turbine wake in the RHI (Range Height Indicator) mode (Kopp et al., 2004; Smalikho et al., 2005), which sweeps elevation angle with a fixed azimuth angle (Kähler  
20 et al., 2010). However, this scanning mode could not always intersect the wake particularly at far wake region due to wake meandering and the variation of wind direction and turbine yaw. Similarly, when lidar operates by sweeping azimuth angle with the constant elevation angle, called Plane Position Indicator (PPI) mode, the distance and orientation from lidar to turbine should be sufficiently far and roughly same with wind direction (Smalikho et al., 2013), respectively. In general, detected wake length is limited by the increasing altitude with range and wake orientation for both PPI and RHI mode of  
25 PCDL. The problem for single ground-based lidar detection is that it can only be used in certain wind direction. Furthermore, analysis of these measurements is based on LOS velocity or simple projection along wake orientation. Vector wind field could be retrieved based on two or more independent measurements (Armijo, 1969; Ray et al., 1978; Rothermel et al., 1985). Three pulsed coherent lidars of Leosphere were employed to deduce the measurements at a fixed point, which was compared with the data collocated from sonic anemometer by Mann et al. (Mann et al., 2009). To  
30 investigate axial and vertical velocity components, simultaneous measurements utilizing two lidars with RHI mode were performed behind a wind turbine by Iungo et al. (Iungo et al., 2013). For this case, one lidar was placed at the turbine location and the other one was located downstream. Hirth et al. employed two radars to reconstruct wake structure, and then discussed the variability of a single turbine wake and the complex flow features included in a wind farm (Hirth and Schroeder, 2013; Hirth et al., 2015).

## 1.1 Velocity deficit and wake length

Definition of velocity deficit at hub height in previous studies can be written as:

$$\delta(x) = \frac{U_{ref}(x) - U_{wake}(x)}{U_{ref}(x)} \times 100\% , \quad (1)$$

where,  $U_{ref}(x)$  is the ambient or reference velocity as a function of longitudinal distance  $x$  downstream from the wind turbine,  $U_{wake}(x)$  is the wake velocity. The initial value depends on the amount of momentum loss induced by wind turbine (Wu et al., 2016), with typical value of approximately 50%–60% (Aitken et al., 2014), 66% in (Kambezidis et al., 1990) and 74% in (Smalikho et al., 2013). Wake length  $L$  is the distance, at which the velocity deficit drops down to 10% (Smalikho et al., 2013), with typical value of 7–10 rotor diameters ( $D$ ) and extreme value of exceeding 20  $D$  (Hirth and Schroeder, 2013) and 30  $D$  (Hirth et al., 2012).

The environmental factors that affect velocity and wake length include wind speed, turbulence, atmospheric stability and surface roughness. Researches indicate that velocity deficit is notably higher at lower ambient velocity owing to higher thrust coefficients (Elliott and Barnard, 1990). It shows that the lowest turbulence intensity occurs at 8–12 $\text{ms}^{-1}$ , in which case the velocity deficit is high due to high turbine thrust coefficient (Elliott and Barnard, 1990; Hansen et al., 2012). Besides, turbulence plays an important role in mixing effect between wake and surrounding air (Aitken et al., 2014), and strongly affects velocity deficit in the far wake (Rhodes and Lundquist, 2013). For instance, Smalikho et al. proposed that wake length would be half when the turbulent energy dissipation rate doubles at high wind speed (Smalikho et al., 2013). In addition, unstable atmospheric conditions would result in the enhancement of turbulence intensity levels. Such as, wind turbine wake recovers faster in convective condition than in neutral condition (Iungo, 2016). However, the factor of surface roughness on wind farm needs more elaborate investigations.

## 1.2 Wake centreline and width

As pointed out by Vermeer et al., downstream wake could be separated into two parts: near and far wake regions, with the dividing line a few  $D$  downwind of the corresponding wind turbine (Vermeer et al., 2003). In the near wake region, the velocity behind the turbine rotor decreases owing to the lift generated along the blade, with a maximum lift value near 75% blade span. Consequently, wind profile of horizontal cross section in the near wake region has two peaks (Smedman, 1998), or double-bell shape (Aitken et al., 2014; Larsen et al., 2007),

$$U(y, r) = U_{ref} - a_1 \times \left\{ \exp \left[ - \left( \frac{y-y_1}{c_1} \right)^2 \right] + \exp \left[ - \left( \frac{y-y_2}{c_1} \right)^2 \right] \right\} , \quad (2)$$

As distance increases downwind, tip vortexes with spirals pattern gradually entwine into one with cross section wind profile of single centreline peak or Gaussian-like shape (Aitken et al., 2014; Larsen et al., 2007),

$$U(y, r) = U_{ref} - a_0 \times \exp \left[ - \left( \frac{y-y_0}{c_0} \right)^2 \right] . \quad (3)$$

In Eq.(2) and Eq.(3)  $U_{ref}$  is the ambient wind speed,  $a_1$  and  $a_0$  are the amplitudes of the Gaussian curve,  $C_1$  and  $C_0$  are the parameters to describe the wake width,  $y_1$ ,  $y_2$  and  $y_0$  are the locations of the left, right and center minima in the double-Gaussian and single-Gaussian curves, respectively. As defined in (Aitken et al., 2014; Hansen et al., 2012), wake width of single-Gaussian shape, with definition of 95% confidence interval of velocity profile, can be written as:

$$5 \quad w_1 = 2\sqrt{2}C_0, \quad (4)$$

while, width of wake with double-Gaussian distribution can be expressed as:

$$w_2 = 2\sqrt{2}C_1 + |y_1 - y_2|, \quad (5)$$

As wake propagates downstream, wake width and centreline behave as in what follows. Due to the mixing effect by small-scale atmospheric eddies (Bingöl et al., 2010), wake expands larger with incremental distance downwind in the horizontal direction than in vertical direction owing to ground effect (Aitken et al., 2014). In addition to wake width, wake centreline shifts upward in the vertical direction due to the larger momentum at the lower part of the wake than in the higher part of the wake (Helmis et al., 1995) and the tilt of the rotor (Aitken et al., 2014). Besides, horizontal displacements of wake centreline are larger than vertical displacements with the ratio of approximately 1.5 (España et al., 2011).

This paper presents characterization of intertidal turbine wakes based on the two pulsed coherent Doppler lidars with a coplanar scanning mode, which can be used for ground-based measurements in condition of various wind directions. In what follows, section 2 describes the methodology of dual-Doppler method and coplanar scanning mode. A coplanar scanning mode to exactly match probing volume is presented in section 3 and applied in field experiments in December, 2014 in section 4. In section 5, observation results, including wakes merging, wake evolution with rising tide and wake meandering, are presented and analysed. Finally, summary and discussion are offered in section 5.

## 20 **2 Methodology**

### **2.1 Principle of dual-Doppler method**

If two or more LOS velocities of a certain probing volume are synchronously detected by independent instruments from different directions, the vector wind at the certain probing volume is possibly derived without assumptions of homogeneous wind field. The principle of dual-Doppler method is described in this section. The geometrical relationship of measuring vector wind ( $\mathbf{V}$ ) at a certain probing volume (denoted by point  $C$ ) with two instruments (denoted by points  $A$  and  $B$ ) is shown in Fig. 1. The detected vertical wind component is neglectable compared with horizontal wind because the detected LOS projection of vertical wind is very small when the transmitting beam emits nearly horizontally. Therefore, for simplification only horizontal wind is considered.

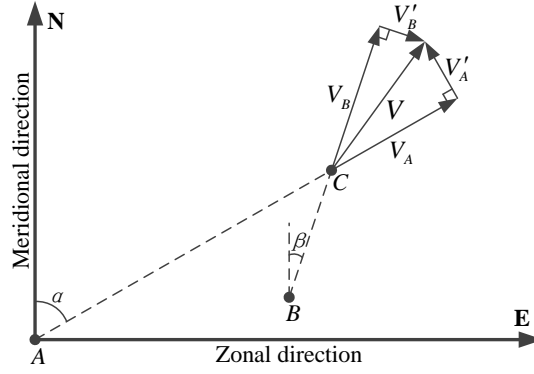


**Figure. 1. Geometrical relationship of measuring vector wind (denoted by  $V$ ) at a certain probing volume (denoted by point  $C$ ) with two instruments (denoted by points  $A$  and  $B$ ) using dual-Doppler method.  $V_A$  and  $V_B$  are LOS components of vector wind  $V$  measured by instruments  $A$  and  $B$ , respectively.  $\alpha$  and  $\beta$  are angles between north and radial direction of instruments  $A$  and  $B$ , respectively.**

As shown in Fig. 1, the position of instrument  $A$  (point  $A$ ) is defined as the origin of geographic coordinate system. X-axis pointing in east indicates zonal direction, while Y-axis pointing in north indicates meridional direction.  $\alpha$  and  $\beta$  are angles between north and radial direction of instruments  $A$  and  $B$ , respectively.  $V_A (u_A, v_A)$  and  $V_B (u_B, v_B)$  are LOS components of vector wind  $V (u, v)$  measured by instruments  $A$  and  $B$ , respectively, which can be expressed as

$$\begin{cases} u_A = V_A \sin \alpha \\ v_A = V_A \cos \alpha \\ u_B = V_B \sin \beta \\ v_B = V_B \cos \beta \end{cases} \quad (6)$$

$V'_A (V'_B)$  is the difference between  $V$  and  $V_A (V_B)$ . Since  $V'_A$  and  $V'_B$  are perpendicular to  $V_A$  and  $V_B$ , respectively, Eq. (7) can be obtained as

$$\begin{cases} u_A \cdot (u - u_A) + v_A \cdot (v - v_A) = 0 \\ u_B \cdot (u - u_B) + v_B \cdot (v - v_B) = 0 \end{cases} \quad (7)$$

The vector wind  $V (u, v)$  at point  $C$  can be derived from Eq. (6) and Eq. (7) as

$$\begin{cases} u = \frac{V_A \cos \beta - V_B \cos \alpha}{\sin(\alpha - \beta)} \\ v = \frac{V_B \sin \alpha - V_A \sin \beta}{\sin(\alpha - \beta)} \end{cases} \quad (8)$$

Subsequently, wind speed  $V$  and wind direction  $\theta$  can be obtained as:

$$V = \sqrt{u^2 + v^2} \quad (9)$$

$$\theta = \begin{cases} \frac{\pi}{2} - \arctan\left(\frac{v}{u}\right), & u > 0 \\ \frac{3\pi}{2} - \arctan\left(\frac{v}{u}\right), & u < 0 \end{cases} \quad (10)$$

After scanning measurements are synchronously performed by two instruments, vector wind filed in overlapped area could be derived without assumption.

## 2.2 Estimation of wind uncertainty

5 In order to evaluate the performance of the measurements based on dual-Doppler method, an estimation of wind uncertainty is presented. According to Eq. (3), the  $u$  and  $v$  components of derived vector wind  $\mathbf{V}$  are functions of four variables,  $\alpha$ ,  $\beta$ ,  $V_A$  and  $V_B$ , as a result the wind uncertainty is contributed from the uncertainty of these four variables. Assuming the pointing error of both instruments is very small during the scanning measurements, the uncertainty of  $\alpha$  and  $\beta$  can be neglected. Considering  $V_A$  and  $V_B$  are measured by different instruments, the uncertainty of  $V_A$  and  $V_B$  should be independent. Therefore, 10 the uncertainty of  $u$  and  $v$  components, denoted as  $\delta u$  and  $\delta v$ , can be expressed by the uncertainty of  $V_A$  and  $V_B$  as

$$\begin{cases} \delta u = \frac{\sqrt{(\cos^2 \beta) \cdot (\delta V_A)^2 + (\cos^2 \alpha) \cdot (\delta V_B)^2}}{|\sin(\alpha - \beta)|} \\ \delta v = \frac{\sqrt{(\sin^2 \beta) \cdot (\delta V_A)^2 + (\sin^2 \alpha) \cdot (\delta V_B)^2}}{|\sin(\alpha - \beta)|} \end{cases}, \quad (11)$$

where,  $\delta V_A$  and  $\delta V_B$  are the uncertainty of  $V_A$  and  $V_B$ . When the instruments used for synchronously scanning measurement have the same measurement uncertainty of LOS velocity,  $\delta V_L = \delta V_A = \delta V_B$ , wind speed uncertainty  $\delta V$  and wind direction uncertainty  $\delta \theta$  can be expressed as

$$15 \quad \delta V = \frac{\sqrt{(\cos^2 \alpha + \cos^2 \beta) \sin^2 \theta + (\sin^2 \alpha + \sin^2 \beta) \cos^2 \theta}}{|\sin(\alpha - \beta)|} \delta V_L, \quad (12)$$

$$\delta \theta = \frac{\sqrt{(\sin^2 \alpha + \sin^2 \beta) \sin^2 \theta + (\cos^2 \alpha + \cos^2 \beta) \cos^2 \theta}}{V |\sin(\alpha - \beta)|} \delta V_L \quad (13)$$

As can be seen from Eq. (12), the uncertainty of wind speed  $\delta V$  is dependent on wind direction and the position of measured point, but is independent of wind speed. Eq. (13) indicates the uncertainty of wind direction  $\delta \theta$  is dependent on wind direction and the position of measured point, and is inversely proportional to wind speed. The item  $|\sin(\alpha - \beta)|$  in both Eq. (12) 20 and Eq. (13) is determined by the position of the measuring point and can be defined as a spatial factor. The spatial factor  $|\sin(\alpha - \beta)|$  approaches zero as the measuring point tends to the line through instruments A and B. In this case, both  $\delta V$  and  $\delta \theta$

increase rapidly, which results in large measurement error. Therefore, the spatial factor can be considered as a reference standard for quality control.

### 3 Coplanar scanning mode

Since the dual-Doppler method requires at least two independent measurements of LOS velocity for retrieving vector wind in each probing volume, higher measurement efficiency can be obtained when a coplanar scan is performed, in which case the intersection of two instruments' scanning surfaces is a plane rather than a curve. Practically, a coplanar scan can be achieved by performing two RHI scans with same azimuth along the line through two instruments (Hill et al., 2010) or two horizontal PPI scans at the same altitude. However, as shown in Fig. 2(a), when two PPI scans with arbitrary elevation are performed, the intersection is a curve. As a result, if a point does not lie on the intersection curve, the altitude difference of these two PPI scans overpassing this position will induce an error in retrieved vector wind (Newsom et al., 2008).

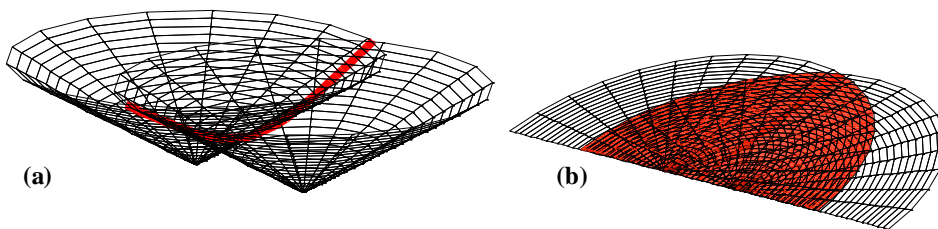


**Figure 2. Schematic of scanning surfaces and intersections of (a) two PPI scans with arbitrary elevation and (b) two PPI scans in a tilted plane. The black grids show the surfaces of PPI scans, and the red line and red area show the intersection curve and the intersection area, respectively.**

A coplanar scanning mode is proposed to achieve vector wind measurements in a certain plane with high efficiency by adjusting the reference planes of two instruments to a same horizontal or tilted plane according to specified requirement, so that a coplanar scanning measurement can be simply achieved by using two instruments to perform synchronous PPI scans with zero elevation in their reference plane. The schematic of the proposed coplanar scanning mode is shown in Fig. 2(b). Practically, the scanning measurement in a tilted plane can be achieved in two ways: by directly performing scanning measurements in the certain plane without tilting the reference plane of instrument or by accordingly tilting the reference plane of instrument and then simply performing scanning measurement in the reference plane. In the first way, both azimuth and elevation of probing beam are correspondingly changing during the entire scanning process so that they have to be accurately controlled. In this case, a smooth planar scan requires high pointing accuracy and controlling performance of scanning mechanism, especially for a lidar system. In the second way, the reference plane of instrument is required to be adjusted from the horizontal plane to the tilted plane, which is operable for a compact lidar system with the help of an AHRS (Attitude and Heading Reference System). After the corresponding attitude, including heading, pitch and roll angles, is calculated and applied, only a simple PPI in the reference plane with zero elevation is need to be performed. In this case,

since the complexity of scanning measurement is significantly reduced, there is no particular requirement in the aspect of instrument mechanism. The strategy of instrument arrangement and the procedure of attitude calculation are described in detail.

For the purpose of simplifying the description and calculating the attitude that needs to be adjusted, both geographic coordinate system and instrument coordinate system are defined. In the geographic coordinate system,  $X$ ,  $Y$  and  $Z$  axes point towards North, East and ground, respectively. In instrument coordinate system, the front, right side and underside of instrument are defined as  $X_0$ ,  $Y_0$  and  $Z_0$  axes, respectively. The azimuth of transmitting beam  $\varphi_0$  is defined as the angle between the projection of transmitting beam on  $X_0$ - $Y_0$  plane and positive  $X_0$  axis. When looking downward,  $\varphi_0$  increases in a clockwise direction. The elevation of transmitting beam  $\theta_0$  is defined as the angle between transmitting beam and  $X_0$ - $Y_0$  plane.

10 The direction of transmitting beam in the instrument coordinate system  $\mathbf{r}_0$  can be expressed by a unit vector as:

$$\mathbf{r}_0 = \begin{pmatrix} x_0 \\ y_0 \\ z_0 \end{pmatrix} = \begin{pmatrix} \cos \theta_0 \cos \varphi_0 \\ \cos \theta_0 \sin \varphi_0 \\ -\sin \theta_0 \end{pmatrix}. \quad (14)$$

The attitude of the instrument can be described by heading, pitch and roll angles which refer to rotations about  $Z_0$ ,  $Y_0$  and  $X_0$  axes, respectively. The unit vector  $\mathbf{r}$  indicates the direction of transmitting beam in geographic coordinate system. The relationship of  $\mathbf{r}_0$  and  $\mathbf{r}$  is:

$$15 \quad \mathbf{r} = (H_1 H_2 H_3)^{-1} \mathbf{r}_0. \quad (15)$$

where,  $H_1$ ,  $H_2$  and  $H_3$  are the rotation matrices of roll  $\varphi$ , pitch  $\theta$  and heading  $\psi$ , respectively, as follows:

$$\left\{ \begin{array}{l} H_1 = \begin{pmatrix} 1 & 0 & 0 \\ 0 & \cos \varphi & \sin \varphi \\ 0 & -\sin \varphi & \cos \varphi \end{pmatrix} \\ H_2 = \begin{pmatrix} \cos \theta & 0 & -\sin \theta \\ 0 & 1 & 0 \\ \sin \theta & 0 & \cos \theta \end{pmatrix} \\ H_3 = \begin{pmatrix} \cos \psi & \sin \psi & 0 \\ -\sin \psi & \cos \psi & 0 \\ 0 & 0 & 1 \end{pmatrix} \end{array} \right. \quad (16)$$

Based on principles of geometry, a plane can be defined by three non-collinear points. Therefore, when the positions of two instruments (points  $A$  and  $B$ ), and the target (point  $C$ ) are selected, the tilted plane in which the coplanar scanning is performed can be determined. Theoretically, when the reference plane of instrument is coincident with the tilted plane, the heading of instrument can be arbitrary, which means the solution of instrument attitude is not unique. A practical way to set

20

up the instruments is to set the  $Y_0$  axis of two instruments to be coincident. In this case, when the reference planes of two instruments are adjusted to the tilted plane, the attitude of two instruments will be uniquely and the same. Moreover, the attitude of both instruments can be simply derived by setting the transmitting beam to two special directions. When the transmitting beam is in the tilted plane and perpendicular to the line through two instruments, the unit vector in instrument coordinate system  $\mathbf{r}_0$  is  $(1, 0, 0)$  and the corresponding unit vector in geographic coordinate system  $\mathbf{r}_1$  is  $(x_1, y_1, z_1)$ . Similarly, when the transmitting beam is along the line through two instruments, the unit vector in instrument coordinate system  $\mathbf{r}_0$  is  $(0, 1, 0)$  and the corresponding unit vector in geographic coordinate system  $\mathbf{r}_2$  is  $(x_2, y_2, z_2)$ . By the way, when the altitude of points  $A$  and  $B$  are approximately same,  $\mathbf{r}_2$  is  $(x_2, y_2, 0)$ . Both  $(x_1, y_1, z_1)$  and  $(x_2, y_2, z_2)$  can be derived from the coordinates of points  $A, B$  and  $C$ . According to the relationship of  $\mathbf{r}_0$  and  $\mathbf{r}$  shown in Eq. (15),  $\mathbf{r}_1$  and  $\mathbf{r}_2$  can be derived as

$$\begin{cases} \mathbf{r}_1 = \begin{pmatrix} x_1 \\ y_1 \\ z_1 \end{pmatrix} = \begin{pmatrix} \cos \psi \cos \theta \\ \sin \psi \cos \theta \\ -\sin \theta \end{pmatrix} \\ \mathbf{r}_2 = \begin{pmatrix} x_2 \\ y_2 \\ z_2 \end{pmatrix} = \begin{pmatrix} \cos \psi \sin \theta \sin \varphi - \sin \psi \cos \varphi \\ \sin \psi \sin \theta \sin \varphi + \cos \psi \cos \varphi \\ \cos \theta \sin \varphi \end{pmatrix} \end{cases} \quad (17)$$

Finally, the heading  $\psi$ , pitch  $\theta$  and roll  $\varphi$  angles of two instruments can be obtained as

$$\begin{cases} \psi = \arctan(y_1/x_1) \\ \theta = -\arcsin z_1 \\ \varphi = \arcsin(z_2/\cos \theta) \end{cases} \quad (18)$$

The measurement target (point  $C$ ) can be either a specified point or the center of an interested volume. Once the target is given, the suitable positions of instruments (points  $A$  and  $B$ ) can be selected according to the terrain and conditions of the site. Usually, the background wind field, detection range of instruments should be taken into consideration as well to reduce measurement uncertainty. At last, the attitude that needs to be adjusted can be derived accordingly. Moreover, when  $z_2$  is zero, roll  $\varphi$  of two instruments is zero according to Eq. (18). In this case, only heading  $\psi$  and pitch  $\theta$  angles of two instruments are needed to adjust and pitch  $\theta$  is the angle of the tilted plane.

#### 4 Description of the experiment

A dual-lidar experiment for measuring wind turbine wakes was performed on December 15, 2014, with cloudy weather condition and westerly to northwesterly wind at the Jiangsu Rudong intertidal wind farm (  $32^{\circ}31'17''$  N,  $121^{\circ}10'32''$  E). Two lidars were deployed on the embankment with the intertidal zone at the top right of the line through two lidars and the coast at the bottom of Fig. 3. The tilted plane scanning mode was adopted for turbine wakes observation with elevation denoted by

the gray contour lines in Fig. 3. The 2-MW wind turbine T1 had a 100-m rotor diameter and a hub height of 80m. The hub height and rotor diameter of the 1.5-MW wind turbine T5, T6 and T7 were 80 m and 93 m, respectively. Two gasoline engine generators were deployed for power supply. Sea Surface Temperature (SST) from European Centre For Medium Range Weather Forecasts (ECMWF) showed that the sea surface temperature was approximately  $10^{\circ}$  which was at least  $4^{\circ}$  higher than the air temperature ( $-1^{\circ}$ – $6^{\circ}$  at local weather station <http://lishi.tianqi.com/rudong/201412.html>). To obtain the rough time when tide began to rise and reached highest point, the tidal level data was achieved from the nearest Yangkou Harbour (<http://www.chinaports.com/chaoxi>), located southeast with a distance of approximately 18 km. Data from the harbour showed that tide began to rise after 1204 local time (LT) with tide height of 222 cm and reached the maximum value of 398 cm at 1811 LT. Accordingly, the tide at the experiment was supposed to be rising from 1300LT to 1700LT.

Two pulsed coherent Doppler lidars (WindPrint S4000) operated are from Seaglet Environmental Technology and modified by Ocean University of China (OUC), with AHRS and GPS (Global Position System) modules to record attitude and position information. Laser pulse width was tuned to 100 ns, corresponding to spatial resolution of 15m in the radial direction. This system has pulse repetition rates of 10 kHz and scanning speed of up to 55 %s, which enables LOS velocity to be measured with temporal resolution of up to 0.25 s. Besides, access to high spatial resolution of up to 15 m during scanning measurements could be provided by the tunable pulse width of 100–400 ns and beam pointing accuracy of  $0.1^{\circ}$ . The component parameters of two systems are given in (Wu et al., 2016). The effective operating range of both lidars were approximately 1.5 km and 2 km, respectively, owing to different optical efficiency between two lidars, which are denoted by shadows as shown in Fig. 1. The contribution of vertical wind component to the measured LOS velocity could be neglected due to the small elevation of laser beams. Wind vector at a certain point could be precisely retrieved from two non-collinear LOS velocities. Therefore, two-dimension vector winds can be obtained by applying this method to the overlap of two scanning ranges.



**Figure 3: Map of the experiment at an intertidal wind farm of Rudong in Jiangsu province of China with the position of wind turbines (denoted by red dots), two scanning lidar (denoted by balloon A and B), the measurement area (denoted by red and green shadows). The gray lines are contours of the tilted measurement plane.**

- 5 The heights of two instruments on the embankment are approximately same and the roll angle of them can be tuned to zero degree. Heading and pitch angle of two lidars were  $28.5^\circ$  and  $4^\circ$ , respectively. Then, the angle of both tilted planes was  $4^\circ$ , adapted to various wind directions and the requirement of obtaining as many wake measurements as possible. In this case, altitude of the tilted plane at wind turbine T1 was about 45m in the low part of wake (wind turbine rotor disk spans a height of 30–130 m). That was favorable to observe the wake in the far wake region because wake decays much more rapidly above
- 10 the hub height than below the corresponding owing to ground effect (Aitken et al., 2014; Elliott and Barnard, 1990). Each scanning took approximately 90 s as the azimuth ranges of two systems were set to  $180^\circ$  with the angular velocity of  $2^\circ \text{ s}^{-1}$  programmed in a script in advance. In practice, the azimuth range could be reduce to  $120^\circ$ , which further reduced the period of each scanning. The effective measurement time ranged from 1020 LT to 1638 LT, which enabled approximately 220 data sets to be collected. Results contaminated by upwind turbines and severe fluctuation of ambient wind field were screened out
- 15 and the rest were analysed in what follows. Quality control procedures were applied to LOS velocity by setting threshold of Signal-to-Noise Ratio (SNR) and effective detection range of 1.5 km for lidar A and 2 km for lidar B, and applied to vector wind by setting the spatial factor  $|\sin(\alpha-\beta)| \geq 0.35$ .

## 5 Results

### 5.1 Wake evolution with rising tide

As mentioned in section 1, turbine wake length  $L$  is defined as the distance where velocity deficit  $\delta(\mathbf{x})$  drops down to 10%. Ambient velocity  $\mathbf{U}_{ref}(\mathbf{x})$  is the upwind velocity (Kähler et al., 2010) or the lateral velocity outside of the wake region (Smalikho et al., 2013). When the wind turbine operates susceptible to others, the ambient velocity is more turbulent and slightly smaller than that in free stream. In this case, the lateral velocity outside of turbine wakes should be taken as ambient velocity. While,  $\mathbf{U}_{wake}(\mathbf{x})$  is the wake velocity along wake orientation. A case of retrieved field is shown in Fig. 4, in which the spatial resolution of wind speed (denoted by colour) is 15m and the corresponding of wind direction (indicated by arrows) is 45m. The wake induced by wind turbine T1 appeared as cooler colours clearly in the downwind direction. Incremental cross sections are plotted as black rectangles and red squares in Fig. 4 to extract ambient and wake velocities shown in Fig. 5 as black crosses and red squares, respectively. And top 5% velocities in each cross section were selected as ambient velocity  $\mathbf{U}_{ref}(\mathbf{x})$  and denoted as black points. The ambient and wake velocities were then averaged by 0.5 D axial bins as black and red triangles. Consequently, the velocity deficit  $\delta(\mathbf{x})$  against the distance downwind was straightforward to be calculated from Eq.(1) as shown in Fig. 6. The velocity deficit did not apparently reduce when  $x \leq 6 D$  due to the increasing altitude along the wake direction, from approximately 45 m to 80 m, resulting in getting close to hub height (relatively higher velocity deficit in vertical direction). By the way, the base of wind turbine T1 located in the intertidal zone was lower than both two lidars, resulting in that the hub height of T1 is slightly lower than 80 m. However when the downstream distance was beyond 6 D, the velocity deficit decreased sharply, partly due to keeping away from hub height.

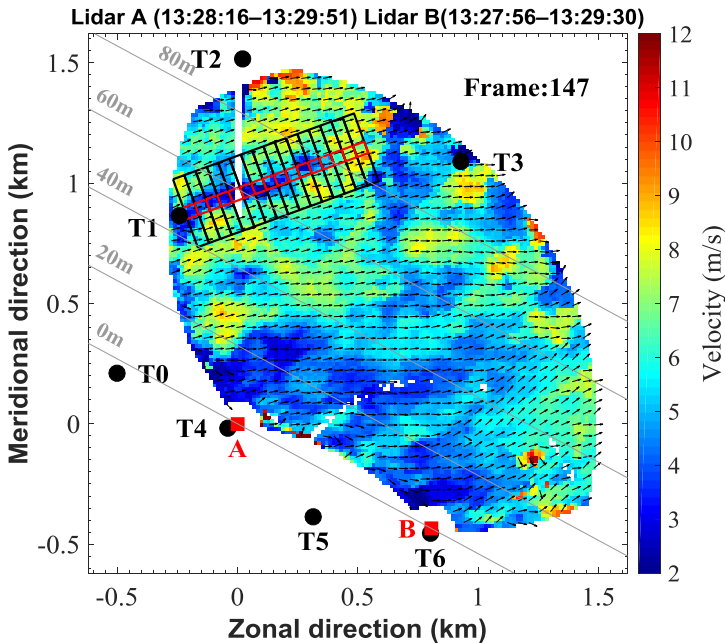


Figure 4: Retrieved vector wind field at intertidal wind farm in China from 1327 LT to 1330 LT on December 15, 2014. The spatial resolution of wind speed is 15m and the corresponding of wind direction is 45m. Red squares and black points indicate two lidars and wind turbine generators, respectively. The gray lines are contours of the titled measurement plane. Velocities in the incremental cross-sections (denoted by red squares and black rectangles) could be extracted to calculate ambient and wake velocities.

5

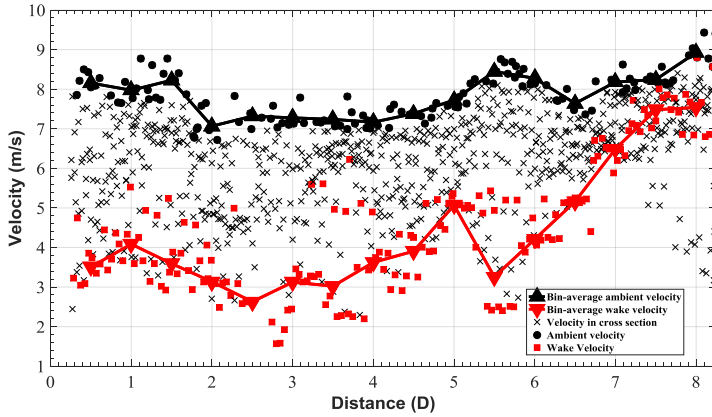
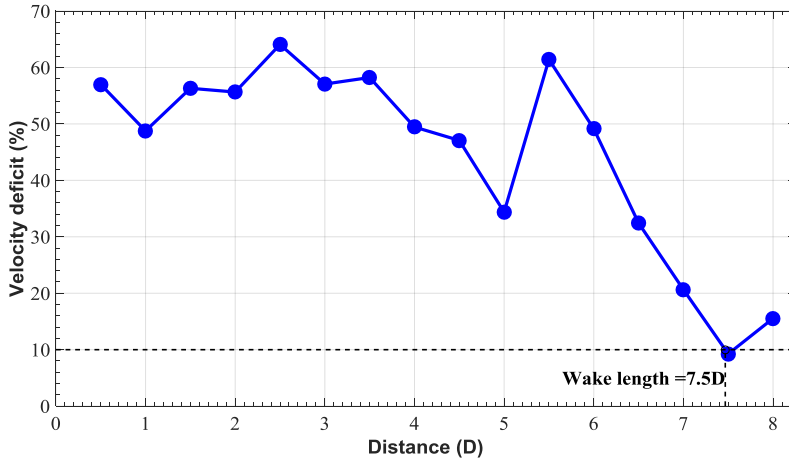


Figure 5: Wind velocities in the incremental cross-sections (as indicated by red squares and black rectangles) are plotted against the distance downwind as red squares, black crosses. The black points are top 5% of black crosses in each cross-section and used as ambient velocities. The red and black triangles are calculated by 0.5 D rang bins.



10

Figure 6: Variation of wake velocity deficit with downstream distance (in the form of rotor diameter D) is indicated by blue points and wake length  $L$  is calculated as the distance where velocity deficit drops down to 10%.

The maximum wind speed and mean wind direction in the altitude of 60 m, 70 m and 80 m were then averaged by 30 min temporal bins as ambient wind speeds and directions shown in Fig. 7(a) and (b) respectively. The turbulence intensity,

15  $I_u = \sigma_u / U$ , could be calculated as the dividing standard deviation of velocity  $\sigma_u$  by the mean of velocity  $U$  and shown in Fig. 7(c). The variation of wake length  $L$  with rising tide could be obtained by applying the method described previously to the wind field results which have clearly visual feature as same as Fig. 3 with a total number of 26, and is shown in Fig. 7(d). Recall that tide rose from approximately 1204LT and reached the maximum level at about 1811LT. At 1525 LT, the

intertidal zone was completely covered by tidewater exactly according to experimental records. The tide rising period ranging from 1230 LT to 1700 LT was divided into two stages. The wake of wind turbine T1 in this period located in the intertidal zone judging from that wind direction veered from southwest (about 220 °) at 1200 LT to west (270 °) at 1413 LT and to northwest (295 °) at 1700 LT.

5 In stage 1 (from 1230 LT to 1525 LT), the underlying surface transformed from mud to sea water and the mean wake length was about 7D with southwesterly wind until 1410 LT. Subsequently, wake length increased to about 10 D at 1415 LT and 11.7 D at 1450 LT with no obvious fluctuation of wind speed ( $9.0 \text{ ms}^{-1}$ – $8.8 \text{ ms}^{-1}$ ) and turbulence intensity (7%–10%) at 80 m height. Typical roughness of flattish ground and ocean surface is approximately 0.03 m and  $<0.001 \text{ m}$  (wind speed  $< 20 \text{ ms}^{-1}$ ), respectively (Emeis, 2012). Accordingly, this wake length increase was primarily caused by the influence of surface  
10 roughness transition.

In stage 2 (from 1525 LT to 1638LT), the hub height relative to the underlying sea surface decreased due to the rising tide with wind speed ranging from  $8.4 \text{ ms}^{-1}$  to  $9.5 \text{ ms}^{-1}$ , wind direction veering from approximately 285 ° to 290 ° and turbulence intensity fluctuating around 10%. The obviously declining to 7.8 D and 8.4 D appeared at 1542 LT and 1546 LT with wake orientation veering from 93 ° to 115 °, respectively, presumably due to that the yaw angle of the wind turbine could not be  
15 tuned immediately to be aligned with ambient wind direction. Despite all this, wake length increased obviously to 15.6 D at 1554 LT with wind speed, wind direction and turbulence intensity of  $9 \text{ ms}^{-1}$ , 285 ° and approximately 10%, respectively, at 80 m height. In this case, underlying surface roughness was not supposed to vary significantly because of no obviously wind speed fluctuating. Therefore, this wake growth was mainly attributed to the tide rising leading to decreased hub height or equivalently enhanced "ground effect", which weakened wake decay in far wake region. It should be pointed out that the the  
20 higher temperature of the sea surface (approximately 10 °) than the air (less than 6 °) may result in surface turbulence which subsequently reduced the wake length by stronger dissipating effect than in stable boundary layer. The unstable air flow possibly led to the wake length reducing to 14.5 D and 13.5 D at 1614 LT and 1616 LT, respectively. However, the wake length still increased to 18D at 1638LT due to rising sea level.

To sum up, the case preliminarily showed that, at least qualitatively, wake length on that day increased in tide rising period  
25 resulting from underlying surface roughness transition, rising sea level.

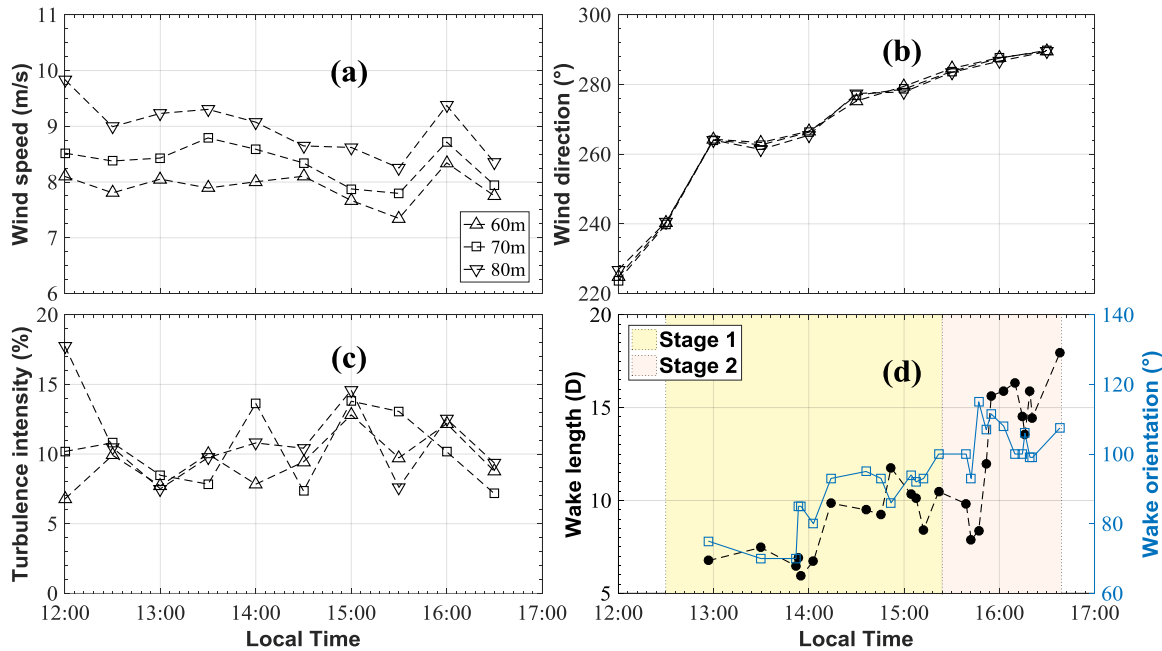


**Figure 7: Variation of ambient wind speed (a), wind direction (b), turbulence intensity (c) and wake length and orientation (d) with rising tide from 1200 LT to 1700 LT. The rising tide period is divided into three stages as shown by different shadows in (d). The wind speed (a), wind direction (b) and turbulence intensity (c) are given in the height of 60 m, 70 m and 80 m.**

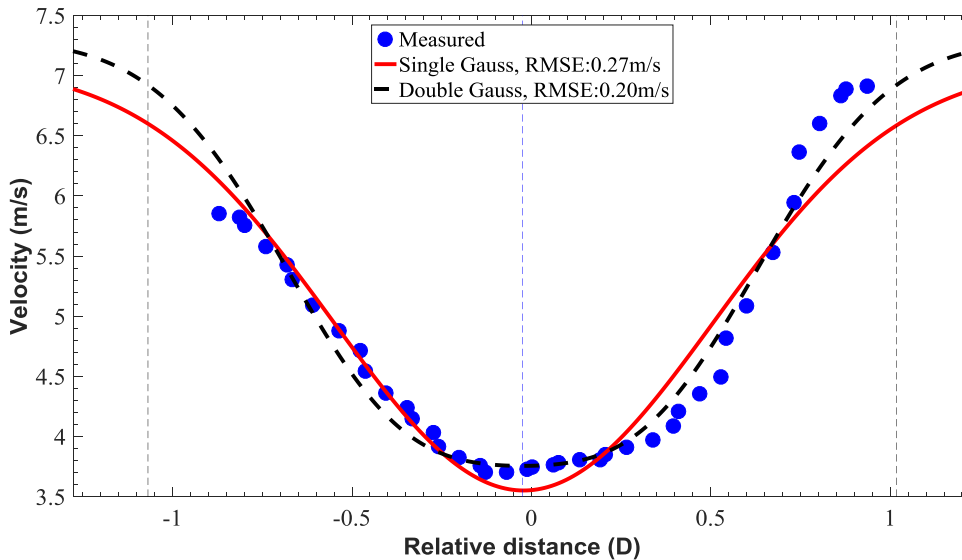
## 5 5.2 Wake meandering

Wake meandering, defined as a random oscillation, is generated and driven when the turbulence length scales are larger than the wake width (España et al., 2011) based on the basic wake meandering model (Bingöl et al., 2010; Larsen et al., 2008). It can be used to evaluate power production, wind turbine loading (Chamorro and Porté-Agel, 2010; Larsen et al., 2008). Significance of wake meandering research lies in its potential for application in optimization of wind farm topology and operation as well as in the optimization of wind turbines for wind farm applications (Larsen et al., 2008). It is shown that wake meandering is greater at higher ambient turbulence intensity conditions (Abkar and Porté-Agel, 2015; Bingöl et al., 2010; Chamorro and Porté-Agel, 2010) and lidar measuring technique could further investigate the fundamental assumption behind the present meandering theory (Larsen et al., 2008).

Since the cross-section wind profile has the distribution of single or double Gaussian shape, wake centre, and width could be subsequently deduced by the least square fit method with single or double Gaussian curve described in section 2. As shown in Fig. 8, wind speed in cross-section as a function of relative distance to wake centre was fitted by the least square method with single and double Gaussian distribution denoted by red and black curves, respectively. While the wake centre was obtained from Eq.(1) and Eq.(2) by a preliminary fit process. The fit was performed iteratively in an attempt to estimate the upper and lower range of variables. However, only one fitted curve with minimum fitting RMSE (root-mean-square error) was adopted to calculate wake centre and width. Then, wake centre line and wake length downwind behind the turbine could

be derived by applying this method to the incremental wake sections. As shown in Fig. 9, wake centre and width are denoted by black lines and points, and the meandering effect could be seen clearly downwind of turbine T1 with approximately 16 D wake length.

As shown in Fig. 10, wake width reduced from 2 D at the distance of  $x=0.5 D$  to 1.4 D at  $x=5 D$  with little variation of wake centre height (about 45 m in Fig. 11), which was most likely relative to the fact that wake centre shifts upward in vertical location (Aitken et al., 2014; Papadopoulos et al., 1995). After 5D, wake meandering was obvious and the height of wake centre would rise due to the result observed in the tilted plane, which could be seen clearly in Fig. 10 that the height of wake centre in tilted plane rose at the distance of  $x > 5D$ . Meanwhile, observed wake width grew to about 4.2 D at approximately 10.5D downwind of T1 arising from that wake expands larger with downwind distance (Aitken et al., 2014). However, wake width fluctuated obviously ranging from 4.2 D to 1.5 D in far wake region as shown in Fig. 10. The main reasons were the turbulence diffusing effect resulting in less precise detection, inherent variability of the wake, as well as the meandering effect (Aitken et al., 2014). It should be pointed out that the observed wake width was unavoidably underestimated compared with the horizontal width across wake centre at hub height because the height of observed wake region (from about 45 m to 65 m) was below hub height (80 m).



15

**Figure 8: Variation of the wind speed (denoted by blue points) in a transect across wind turbine wake as a function of the distance from the center of the wake, are fitted by single Gaussian (red curve) and double Gaussian (black dash curve) curves, respectively.**

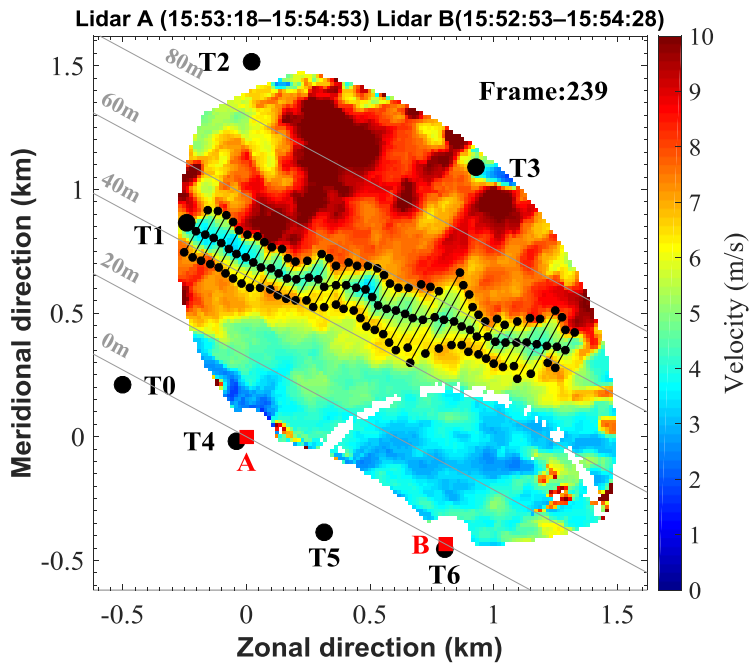


Figure 9: Retrieved wind speed (with spatial resolution of 15 m) by two synchronously scanning lidars (denoted by red squares) around wind turbines (denoted by black points). Centre line and width (in the titled plane) of the wake behind wind generator T1 are denoted by black points and lines, respectively.

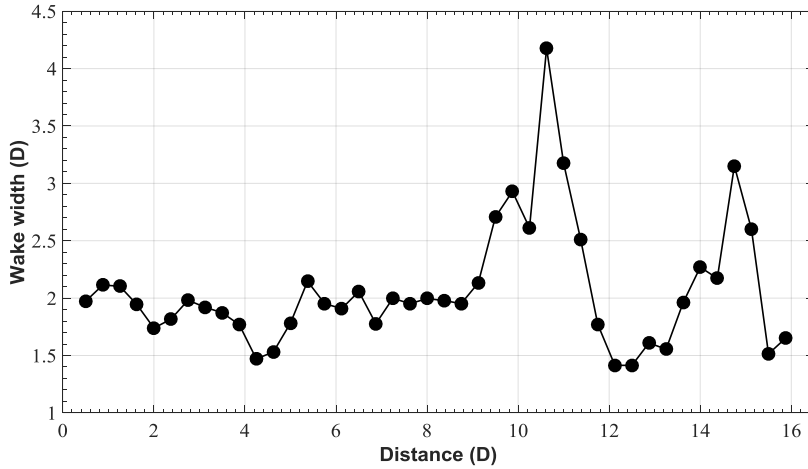
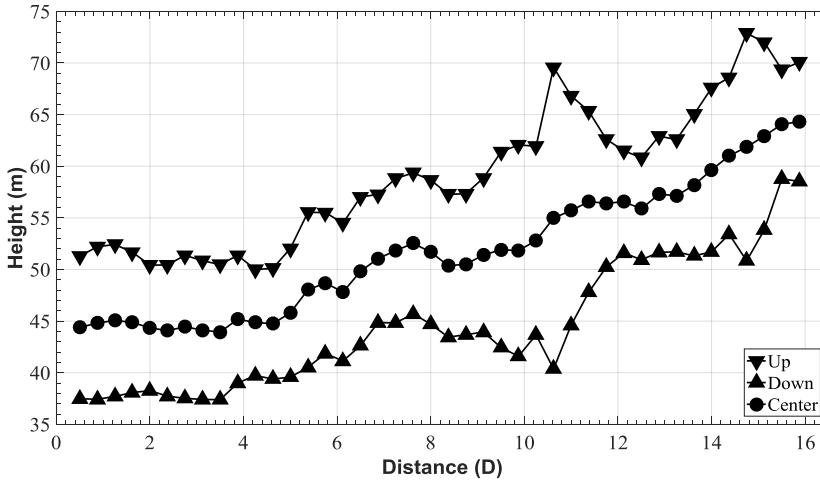


Figure 10: Variation of wake width in the titled plane with downstream distance from wind turbine generator T1

5



**Figure 11: Height of wake boundary (up and down parts in tilted plane) and centreline observed in tilted plane.**

Statistics of the wake centrelines is shown in Fig. 12 and the displacement to lateral distance against increasing wake axial distance is irregular with assumption of Gaussian frequency distribution in horizontal lateral direction  $y$  (Högström et al., 1988):

$$f = A \exp\left(-\frac{y^2}{2\sigma_c^2}\right), \quad (6)$$

while,  $f$  has the normalizing requirement,

$$\int_{-\infty}^{\infty} f(y) dy = 1, \quad (7)$$

and  $\sigma_c$  is the standard deviation of Gaussian frequency distribution with linear increase at longitudinal distance  $x \leq 1 \text{ km}$  downstream of the wind turbine:

$$\sigma_c = kx, \quad (8)$$

where,  $k$  is the slope value with 0.053 in (Högström et al., 1988). Subsequently, the standard deviation of wake centreline displacement was calculated and presented in Fig. 13 as black squares. The linear relationship between longitudinal distance  $x$  and  $\sigma_c$  was calculated by linear fitting and indicated as blue line in Fig. 13 with slope value of 0.057, which was slightly larger than 0.053 presumably due to stronger mesoscale wind fluctuations (Högström et al., 1988). However when longitudinal distance exceeded 10 D, the nonlinear relationship was obvious that  $\sigma_c$  has the similarly exponential increase and expressed as red curve in Fig. 13. That would be the main reason why the wake lengths observed by in situ measurements were less than by other remote sensing instruments.

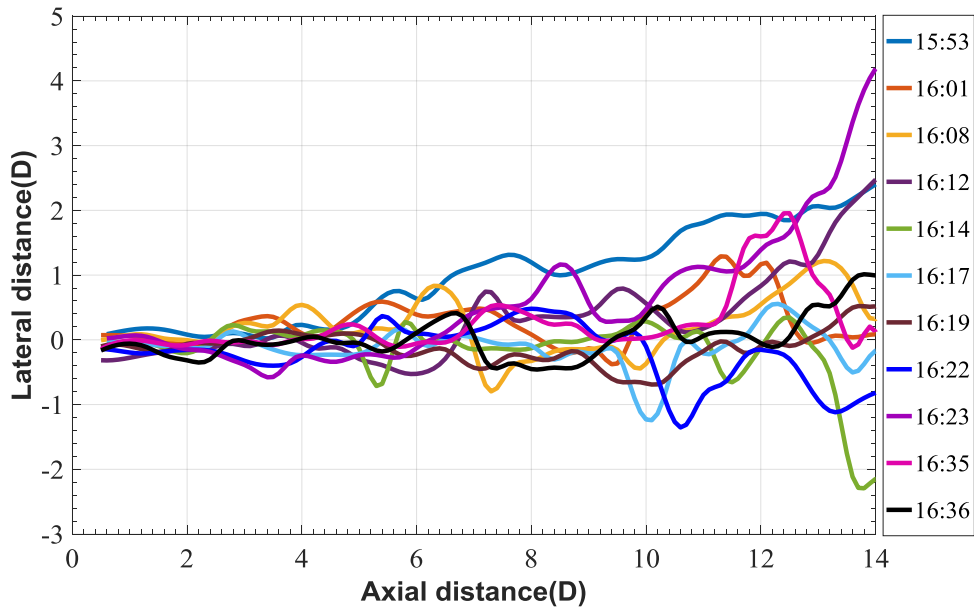
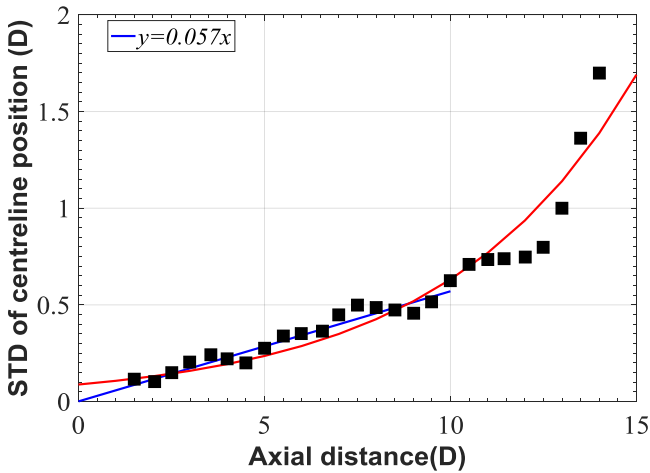


Figure 12: Statistics of wake centrelines displacement in lateral direction along wake axial distance



5 Figure 13: Standard deviation of centreline position as a function of axial distance in wake direction, the black squares are calculated from Figure 12, the blue line indicates the linear fit at the distance of <1 km (10 D). The red curve represents exponential increase in the range of <14 D.

## 6 Conclusions

In this study, we analyze wind turbine wake in the intertidal zone analysis based on the dual-Doppler method with a coplanar  
 10 plane scanning strategy. The conclusions drawn are in what follows.

The dual-lidar technology with designed coplanar scanning mode could be properly applied in the situation of variable wind direction compared with traditional PPI or RHI scanning mode, in which the lidar-turbine line should be strictly aligned or roughly same with the turbine wake. Besides, wake analysis could be directly based on retrieved wind field, which is more convenient than LOS velocity or projection along wake direction utilizing only one lidar system. The inclination angle of the tilted plane was tuned to  $4^\circ$ . In this case the altitude of the wind turbine T1 was approximately 45 m and below hub height of 80 m, which was favorable to observe the far wake region to some extent. The pointing accuracy of the lidar beam scanner and the temporal difference of two LOS velocities at the same points should be further taken into account, which can be optimized by reducing angular velocity and scanning a specific wake region, respectively. However, the ideal mounting location of lidar is on the nacelles, in which case wake structure in horizontal and vertical direction at hub height could be scanned by PPI with zero elevation angle and RHI mode transecting the wake centreline due to lidar yawing along with the wind turbine. This method is an improvement for ground-based measurements.

The case analysis showed that wake length on that day evolved with rising tide at least qualitatively due to the impact of underlying surface roughness transition and rising sea level on the wake. Variation of wind speed and turbulence is not obvious, but the wind direction veered from southwest to northwest. The observation range is limited when wind blowed from southwest. However, there was no case of wake length beyond the observation range in all measurements. It is necessary to carry out on several periods of wake measurements for each set of turbines with similar characteristics (hub-height, rotor diameter, wake fetch etc). Wake meandering case was also analysed based on the characteristic of the cross-section velocity distribution.

The previous method of velocity deficit calculation might be affected by the meandering especially in the far wake region as the selected wake regions deviate from the wake centreline. Nevertheless, as the wake propagated downstream and was mixed by small-scale ambient turbulence, it was difficult to distinguish the centreline of sufficiently dissipated wake. Moreover, the wake meandering introduced a new problem of whether the wake length was calculated by the wake centreline length or the length from wake centreline to the wind turbine. Besides, wake meandering is a random oscillation as mentioned above, which seemed to have no relationship with rising tide. By considering all these, the severe meandering wakes were ruled out in the wake length calculation for simplification.

Both sides of the observed ambient velocities outside of the wake were different due to the tilted plane resulting in different heights, which would cause asymmetry double Gaussian curve and further bring large bias of wake centre and width. As a result, the length of the cross-section should be narrow enough. However to guarantee the fitting precision, more data points means longer cross-section. Accordingly, the adopted length of cross-section was a tradeoffs between both requirements.

In summary, wake behaviour could be properly observed based on the dual-lidar method for its feasibility in variety wind direction. But the more ideal mounting location of lidar is on the nacelles. Besides, further field experiments shall be performed to quantify the dependence of the wake behaviour (velocity deficit, wake length, wake boundary and wake centreline) on the atmospheric condition (wind speed, turbulence, surface roughness and atmospheric stability) combined with turbine model, and ultimately improve the prediction of wind power harvesting.

## Acknowledgement

We thank our colleagues for their kind support during the field experiments and results discussion, including Quanfeng Zhuang, Guining Wang and Xiaoqing Yu from Ocean University of China (OUC) for the preparing and conducting the experiment; Yilin Qi and Jie Bai from Seaglet Environment Technology for preparing and operating the lidar in the cold and  
5 windy wind farm. This work was partly supported by the National Natural Science Foundation of China (NSFC) under grant 41471309 and 41375016.

## References

- Abkar, M. and Porté-Agel, F.: Influence of atmospheric stability on wind-turbine wakes: A large-eddy simulation study, *Physics of Fluids* (1994-present), 27, 19, 2015.
- 10 Aitken, M. L., Banta, R. M., Pichugina, Y. L., and Lundquist, J. K.: Quantifying wind turbine wake characteristics from scanning remote sensor data, *Journal of Atmospheric and Oceanic Technology*, 31, 765-787, 2014.
- Aitken, M. L. and Lundquist, J. K.: Utility-scale wind turbine wake characterization using nacelle-based long-range scanning lidar, *Journal of Atmospheric and Oceanic Technology*, 31, 1529-1539, 2014.
- 15 Armijo, L.: A theory for the determination of wind and precipitation velocities with Doppler radars, *Journal of the Atmospheric Sciences*, 26, 570-573, 1969.
- Anderson, J. W. and Clayton, G. M.: Lissajous-like scan pattern for a gimbaled LIDAR, 2014, 1171-1176.
- Baker, R. W. and Walker, S. N.: Wake measurements behind a large horizontal axis wind turbine generator, *Solar Energy*, 33, 5-12, 1984.
- Barthelmie, R., Folkerts, L., Ormel, F., Sanderhoff, P., Eecen, P., Stobbe, O., and Nielsen, N.: Offshore wind turbine wakes measured by SODAR, *Journal of Atmospheric and Oceanic Technology*, 20, 466-477, 2003.
- 20 Barthelmie, R. J. and Jensen, L.: Evaluation of wind farm efficiency and wind turbine wakes at the Nysted offshore wind farm, *Wind Energy*, 13, 573-586, 2010.
- Bingöl, F., Mann, J., and Larsen, G. C.: Light detection and ranging measurements of wake dynamics part I: one - dimensional scanning, *Wind energy*, 13, 51-61, 2010.
- Chamorro, L. P. and Porté-Agel, F.: Effects of thermal stability and incoming boundary-layer flow characteristics on wind-turbine wakes: a wind-tunnel study, *Boundary-layer meteorology*, 136, 515-533, 2010.
- 25 Chowdhury, S., Zhang, J., Messac, A., and Castillo, L.: Unrestricted wind farm layout optimization (UWFLO): Investigating key factors influencing the maximum power generation, *Renewable Energy*, 38, 16-30, 2012.
- Elliott, D. and Barnard, J.: Observations of wind turbine wakes and surface roughness effects on wind flow variability, *Solar Energy*, 45, 265-283, 1990.
- 30 Emeis, S.: *Wind energy meteorology: atmospheric physics for wind power generation*, Springer Science & Business Media, 2012.
- España, G., Aubrun, S., Loyer, S., and Devinant, P.: Spatial study of the wake meandering using modelled wind turbines in a wind tunnel, *Wind Energy*, 14, 923-937, 2011.
- Fuertes, F. C., Iungo, G. V., and Porté-Agel, F.: 3D Turbulence Measurements Using Three Synchronous Wind Lidars: Validation against Sonic Anemometry, *Journal of Atmospheric and Oceanic Technology*, 31, 1549-1556, 2014.
- 35 Hansen, K. S., Barthelmie, R. J., Jensen, L. E., and Sommer, A.: The impact of turbulence intensity and atmospheric stability on power deficits due to wind turbine wakes at Horns Rev wind farm, *Wind Energy*, 15, 183-196, 2012.
- Helmis, C., Papadopoulos, K., Asimakopoulos, D., Papageorgas, P., and Soilemes, A.: An experimental study of the near-wake structure of a wind turbine operating over complex terrain, *Solar Energy*, 54, 413-428, 1995.
- Hill, M., Calhoun, R., Fernando, H., Wieser, A., D'Amico, A., Weissmann, M., Mayr, G., and Newsom, R.: Coplanar Doppler lidar retrieval of rotors from T-REX, *Journal of the Atmospheric Sciences*, 67, 713-729, 2010.
- 40 Hirth, B. D. and Schroeder, J. L.: Documenting wind speed and power deficits behind a utility-scale wind turbine, *Journal of Applied Meteorology and Climatology*, 52, 39-46, 2013.
- Hirth, B. D., Schroeder, J. L., Gunter, W. S., and Guynes, J. G.: Coupling Doppler radar - derived wind maps with operational turbine data to document wind farm complex flows, *Wind Energy*, 18, 529-540, 2015.
- 45 Hirth, B. D., Schroeder, J. L., Gunter, W. S., and Guynes, J. G.: Measuring a utility-scale turbine wake using the TTUKa mobile research radars, *Journal of Atmospheric and Oceanic Technology*, 29, 765-771, 2012.
- Högström, U., Asimakopoulos, D., Kambezidis, H., Helmis, C., and Smedman, A.: A field study of the wake behind a 2 MW wind turbine, *Atmospheric Environment* (1967), 22, 803-820, 1988.

- Jungo, G. V.: Experimental characterization of wind turbine wakes: Wind tunnel tests and wind LiDAR measurements, *Journal of Wind Engineering and Industrial Aerodynamics*, 149, 35-39, 2016.
- Jungo, G. V., Wu, Y.-T., and Porté-Agel, F.: Field measurements of wind turbine wakes with lidars, *Journal of Atmospheric and Oceanic Technology*, 30, 274-287, 2013.
- 5 Kambezidis, H., Asimakopoulos, D., and Helmis, C.: Wake measurements behind a horizontal-axis 50 kW wind turbine, *Solar & wind technology*, 7, 177-184, 1990.
- Käslér, Y., Rahm, S., Simmet, R., and Kühn, M.: Wake measurements of a multi-MW wind turbine with coherent long-range pulsed Doppler wind lidar, *Journal of Atmospheric and Oceanic Technology*, 27, 1529-1532, 2010.
- Kopp, F., Rahm, S., and Smalikho, I.: Characterization of aircraft wake vortices by 2- $\mu$ m pulsed Doppler lidar, *Journal of Atmospheric and Oceanic Technology*, 21, 194-206, 2004.
- 10 Larsen, G. C., Madsen Aagaard, H., Bingöl, F., Mann, J., Ott, S., Sørensen, J. N., Okulov, V., Troldborg, N., Nielsen, N. M., and Thomsen, K.: Dynamic wake meandering modeling, *Risø National Laboratory*8755036023, 2007.
- Larsen, G. C., Madsen, H. A., Thomsen, K., and Larsen, T. J.: Wake meandering: a pragmatic approach, *Wind energy*, 11, 377-395, 2008.
- Mann, J., Cariou, J. P., Courtney, M. S., Parmentier, R., Mikkelsen, T., Wagner, R., Lindelow, P., Sjöholm, M., and Enevoldsen, K.: 15 Comparison of 3D turbulence measurements using three staring wind lidars and a sonic anemometer, *Meteorologische Zeitschrift*, 18, 135-140, 2009.
- Newsom, R., Calhoun, R., Ligon, D., and Allwine, J.: Linearly organized turbulence structures observed over a suburban area by dual-Doppler lidar, *Boundary-layer meteorology*, 127, 111-130, 2008.
- Papadopoulos, K., Helmis, C., Soilemes, A., Papageorgas, P., and Asimakopoulos, D.: Study of the turbulent characteristics of the near-wake field of a medium-sized wind turbine operating in high wind conditions, *Solar Energy*, 55, 61-72, 1995.
- 20 Porté-Agel, F., Wu, Y.-T., Lu, H., and Conzemius, R. J.: Large-eddy simulation of atmospheric boundary layer flow through wind turbines and wind farms, *Journal of Wind Engineering and Industrial Aerodynamics*, 99, 154-168, 2011.
- Ray, P. S., Wagner, K., Johnson, K., Stephens, J., Bumgarner, W., and Mueller, E.: Triple-Doppler observations of a convective storm, *Journal of Applied Meteorology*, 17, 1201-1212, 1978.
- 25 Rhodes, M. E. and Lundquist, J. K.: The effect of wind-turbine wakes on summertime US Midwest atmospheric wind profiles as observed with ground-based doppler lidar, *Boundary-Layer Meteorology*, 149, 85-103, 2013.
- Rothermel, J., Kessinger, C., and Davis, D. L.: Dual-Doppler lidar measurement of winds in the JAWS experiment, *Journal of Atmospheric and Oceanic Technology*, 2, 138-147, 1985.
- Smalikho, I., Banakh, V., Pichugina, Y., Brewer, W., Banta, R., Lundquist, J., and Kelley, N.: Lidar investigation of atmosphere effect on a wind turbine wake, *Journal of Atmospheric and Oceanic Technology*, 30, 2554-2570, 2013.
- 30 Smalikho, I., Kopp, F., and Rahm, S.: Measurement of atmospheric turbulence by 2- $\mu$ m Doppler lidar, *Journal of Atmospheric and Oceanic Technology*, 22, 1733-1747, 2005.
- Smedman, A.-S.: Air Flow Behind Wind Turbines, *Journal of Wind Engineering and Industrial Aerodynamics*, 80, 169-189, 1998.
- Trujillo, J. J., Bingöl, F., Larsen, G. C., Mann, J., and Kühn, M.: Light detection and ranging measurements of wake dynamics. Part II: 35 two - dimensional scanning, *Wind Energy*, 14, 61-75, 2011.
- Vermeer, L., Sørensen, J. N., and Crespo, A.: Wind turbine wake aerodynamics, *Progress in aerospace sciences*, 39, 467-510, 2003.
- Wu, S., Liu, B., Liu, J., Zhai, X., Feng, C., Wang, G., Zhang, H., Yin, J., Wang, X., Li, R., and Gallacher, D.: Wind turbine wake visualization and characteristics analysis by Doppler lidar, *Opt. Express*, 24, 19, 2016.
- 40 Wu, S., Yin, J., Liu, B., Liu, J., Li, R., Wang, X., Feng, C., Zhuang, Q., and Zhang, K.: Characterization of turbulent wake of wind turbine by coherent Doppler lidar, 2014, 92620H-92620H-92610.
- Wu, Y.-T. and Porté-Agel, F.: Atmospheric turbulence effects on wind-turbine wakes: An LES study, *energies*, 5, 5340-5362, 2012.